The 8th European Congress on Computational Methods in Applied Sciences and Engineering
ECCOMAS Congress 2022
5-9 June 2022, Oslo, Norway

THE INFLUENCE OF THE TRACER PLACEMENT ON SEA ICE DEFORMATION FIELDS

Carolin Mehlmann[1], Sergey Danilov[2]

[1] Institute of Analysis and Numerics
Otto-von-Guericke-Universitt
Universittsplatz 2, 39106 Magdeburg, Germany
e-mail: carolin.mehlmann@ovgu.de

[2] Alfred-Wegener-Institut, Helmholtz Zentrum fr Polar- und Meeresforschung, Am Handelshafen 12,
27570 Bremerhaven, Germany
email: sergey.danilov@awi.de,

Key words: Finite elements, triangular meshes, sea ice dynamics

Abstract. Sea ice models can simulate linear deformation characteristics (linear kinematic features) that are observed from satellite imagery. A recent study based on the viscous-plastic sea ice model highlights the role of the velocity placement on the simulation of linear kinematic features (LKFs) and concluded that the tracer staggering has a minor influence on the amount simulated LKFs. In this work we consider the same finite element discretization and show that on triangular meshes the placement of the sea ice tracers and the associated degrees of freedom (DoFs) have a strong influence on the amount of simulated LKFs. This behaivor can be explained by the change of the total number of DoFs associated with the tracer field. We analyze the effect on a benchmark problem and compare P1-P1, P0-P1, CR-P0 and CR-P1 finite element discretizations for the velocity and the tracers, respectively. The influence of the tracer placement is less strong on quadrilateral meshes as a change of the tracer staggering does not modify the total number of DoFs. Among the low order finite element approximations compared in this study, the CR-P0 finite element discretization resolves the deformation structure in the best way. The CR finite element for velocity in combination with the P0 discretization for tracer produces more LKFs than the P1-P1 finite element pair even on grids with fewer DoFs. This can not be achieved with the CR-P1 setup and therefore highlights the importance of the tracer discretization for the simulation of LKFs on triangular meshes.

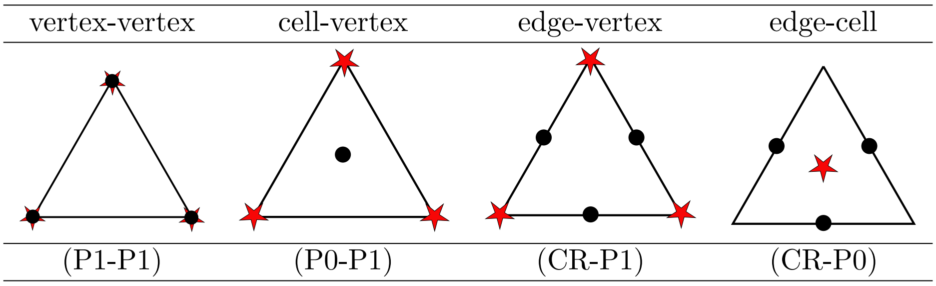

Figure 1: The placement of the velocity $\mathbf{v}$ and the tracers are indicated by $\bullet$, and $\star$, respectively. The upper row names the position of the velocity and the tracers on the mesh, whereas the lower row indicates the corresponding finite element discretization. P1, P0 and CR refers to the piecewise linear, the piecewise constant and nonconforming linear (Crouzeix-Raviart) element. The visualization of P1-P1, P0-P1 and CR-P0 has been used in [17].

1 Introduction

Satellite imagery of polar regions shows that the sea ice cover is characterized by local linear deformations called linear kinematic features (LKFs). During drift sea ice deforms in response to internal stresses and forcing such that linear kinematic features can be build. LKFs play an important role in sea ice formation and in the interaction between ocean and atmosphere [9]. Furthermore the location and width of the LKFs is crucial for the Arctic shipping [19].

To simulate LKFs in sea ice models the description of the internal stress is central. In continuum sea ice models the internal stresses are prescribed by the sea ice rheology. So far most climate models characterize sea ice as a viscous-plastic material using either the classical viscous-plastic formulation [10] or the elastic-viscous-plastic approximation [11]. In the last years alternative rheologies have been developed (e.g [7, 8, 21, 23]). Nevertheless, the (E)VP model will be used in the foreseeable future, which motivates our research on this topic.

Viscous-plastic sea ice model are capable to simulate LKFs once the spatial resolution is high enough [12, 22]. In this model sea ice is characterized by a velocity, the thickness and the concentration of ice. The later two quantities are the tracers of the model. Using the viscous-plastic sea ice model a recent study analyzed the influence of velocity placement on the formation of LKFs [17]. The analysis shows that the velocity staggering has a strong influence on the number and the total length of resolved LKFs. The study demonstrates that the placement of the velocity on edges instead of currently used cell or vertex staggering increases the amount of resolved LKFs. One reason for the improved resolving capacity is the higher number of degrees of freedom in the velocity field which is achieved by placing the velocity vector onto the edge midpoint instead of the vertex or the center of a grid cell. The higher total number of degrees of freedom in the velocity field leads to a sharper representation of gradients and strain rates. Based on the results obtained on quadrilateral meshes the study concludes that the tracer staggering has a minor influence on the formation of LKFs.

In this contribution we will revise this finding and analyze the influence of the tracer placement on the formation of LKFs on triangular meshes using the same finite element pairs as in the study of [17]. For simplicity we refer to the P1-P1, P0-P1, CR-P0 and CR-P1 finite element as the *vertex-vertex*, *cell-vertex*, *edge-cell* and *edge-vertex* staggering. The first part of the pairs refers to the velocity disctretization and the second term indicates the tracer treatment. P1 is the piecewise linear element, P0 refers to the piecewise constant element [2] and CR denotes the nonconforming linear element (Crouzeix-Raviart element) [4]. The different discretizations are visualized in Figure 1.

Currently the vertex-vertex placement is used in the *Finite-Volume Sea IceOcean Model* (FESOM)[6], the cell-vertex staggering is applied in *Model for Prediction Across Scales* (MPAS)[20], while the edge-cell discretization is used in the sea ice module of the *Icosahedral Nonhydrostatic Weather and Climate Model* (ICON)[15, 18].

On triangular meshes, in contrast to the quadrilateral case, the tracer placement changes the total amount of degrees of freedom (DoFs). The DoFs depend on the position of the tracer on a triangle. They are defined by the numbers of vertices, cells and edges of the considered mesh. As the tracer placement is directly related to the resulting internal stress through the ice strength, the increased amount of DoFs has an effect on the deformation field on a fixed grid level. To examine the effect we evaluate the simulations of a recently defined benchmark problem [17]. The simulations are performed in the framework of FESOM [6]. Please note that the data of P1-P1, P0-P1 and CR-P0 has already been used in the study in [17].

The paper is structured as follows. Section 2 presents the viscous-plastic sea ice model and describes the numerical discretizations. The benchmark problem and the numerical results are presented in Section 3 and discussed in Section 4.

2 The viscous-plastic sea ice model and the numerical discretization

In our study we use a simplified model of the sea ice dynamics, where sea ice is modeled by three variables: the sea ice concentration c, the mean sea ice thickness h and the sea ice velocity $\mathbf{v}$. The sea ice dynamics are described by the following system of coupled partial differential equations.

$$m_{\text{ice}}\partial_t \mathbf{v} = \mathbf{F}, \tag{1}$$

$$\partial_t c + \operatorname{div}(\mathbf{v}c) = 0, \quad c \leq 1, \tag{2}$$

$$\partial_t h + \operatorname{div}(\mathbf{v}h) = 0. \tag{3}$$

The mass is given by $m_{\text{ice}} = \rho_{ice} h$, where $\rho_{ice} = 900\,\text{kg/m}^3$ is the ice density. The forces acting on sea ice are collected in

$$\mathbf{F} = -f_c \boldsymbol{e}_r \times \mathbf{v} + \operatorname{div} \boldsymbol{\sigma} + c\boldsymbol{\tau}(\mathbf{v}) - m_{\text{ice}} g \nabla \tilde{H}_g, \tag{4}$$

where $f_c = 1.46 \cdot 10^{-4}\,\text{s}^{-1}$ is the Coriolis parameter and $\boldsymbol{e}_z$ describes the vertical (z-direction) unit vector. The influence of the changing sea surface height $\tilde{H}_g$ can be approximated as

$$m_{\text{ice}} g \nabla \tilde{H}_g \approx -m_{\text{ice}} f_c \boldsymbol{e}_r \times \mathbf{v}_w, \tag{5}$$

where $\mathbf{v}_w$ is the ocean velocity [3]. $\boldsymbol{\tau}(\mathbf{v})$ models the ocean and atmospheric surface stresses

$$\boldsymbol{\tau}(\mathbf{v}) = C_w \rho_w |\mathbf{v}_w - \mathbf{v}|_2 (\mathbf{v}_w - \mathbf{v}) + C_a \rho_a |\mathbf{v}_a|_2 \mathbf{v}_a, \tag{6}$$

with the wind velocity $\mathbf{v}_a$, the drag coefficents $C_w = 5.5 \cdot 10^{-3}, C_a = 1.2 \cdot 10^{-3}$ and the water and air densties $\rho_w = 1026\,\mathrm{kg/m^3}$ and $\rho_a = 1.3\,\mathrm{kg/m^3}$. The internal force applied to the ice drift are modeled by $\mathrm{div}(\boldsymbol{\sigma})$. The relation of the stresses $\boldsymbol{\sigma}$ and the strain rates, $\dot{\boldsymbol{\epsilon}} = (1/2)(\nabla\mathbf{v} + \nabla\mathbf{v}^T)$, are given by the the viscous-plastic (VP) material law. The superscript T indicates the transposed quantity. The VP rheology developed by Hibler [10] reads as

$$\boldsymbol{\sigma} = 2\eta\dot{\boldsymbol{\epsilon}} + (\zeta - \eta)\,\mathrm{tr}(\dot{\boldsymbol{\epsilon}})I - \frac{P}{2}I, \tag{7}$$

with I the identity matrix and the shear and bulk viscosities η and ζ,

$$\eta = e^{-2}\zeta, \quad \zeta = \frac{P_0}{2\Delta(\dot{\boldsymbol{\epsilon}})}, \quad \Delta(\dot{\boldsymbol{\epsilon}}) = \sqrt{\dot{\boldsymbol{\epsilon}}_I^2 + e^{-2}\dot{\boldsymbol{\epsilon}}_{II}^2 \Delta_{\min}^2}. \tag{8}$$

$e = 2$ is the ratio of the semiaxes of elliptic yield curve and $\Delta_{\min} = 2 \cdot 10^{-9}\,\mathrm{s^{-1}}$ is the threshold that describes the transition from the viscous and the plastic material state. The invariant $\dot{\boldsymbol{\epsilon}}_I = \mathrm{tr}(\dot{\boldsymbol{\epsilon}})$ models the compression and tension, while $\dot{\boldsymbol{\epsilon}}_{II}$ is the shear deformation. The latter is given as

$$\dot{\boldsymbol{\epsilon}}_{II} = \Big[\Big(\dot{\boldsymbol{\epsilon}}_{11} - \dot{\boldsymbol{\epsilon}}_{22}\Big)^2 - 4\big(\dot{\boldsymbol{\epsilon}}_{12}\big)^2\Big]^{\frac{1}{2}}. \tag{9}$$

The ice strength P in (7) is modeled as

$$P = P_0 \frac{\Delta(\dot{\boldsymbol{\epsilon}})}{(\Delta(\dot{\boldsymbol{\epsilon}}) + \Delta_{\min})}, \quad P_0(h, c) = P^{\star} h \exp\big(-20(1-c)\big), \tag{10}$$

with the ice strength parameter $27.5 \cdot 10^3\,\mathrm{N/m^2}$.

This coupled system of partial differential equations is discretized as follows. The momentum equation (1) is treated in space with finite elements (P1 or CR), and finite volumes in case of P0. The CR setup requires a stabilization due to instabilities which arise from the discretization of the symmetric strain rate tensor of the sea ice rheology. More details on the stabilization can be found in [18]. The P0 discretization also suffers from instabilities in the velocity field if strain rates are computed at vertices. We stabilized the approximation by reconstructing the strain rates at the element-edge, see [5] for further details. The momentum equation is integrated forward with an explicit pseudo time-stepping scheme. The so called mEVP solver [1] is used. The detailed configuration of the method is outlined in [5]. We perform $M = 100$ sub-cycle steps per external time step. The iteration number M is chosen in such a way that the number of sub-iterations does not influence the simulated total length of LKFs detected by an image recognition algorithm [14]. The transport equation are discretized either with P1 or P0 finite elements. In case of the P1 disctrization the sea ice thickness and concentration is advected with a Taylor-Galerkin flux-corrected transport method [16], whereas the P0 setup uses an upwind scheme.

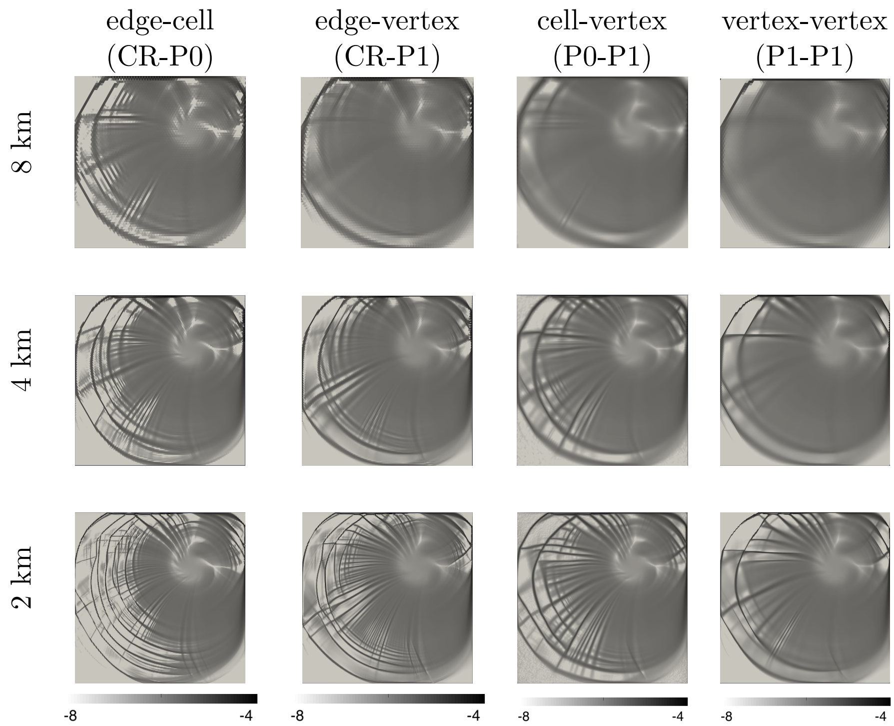

Figure 2: Shear deformation plotted in a logarithmic scale. Note that the visualization of P1-P1, P0-P1 and CR-P0 on 4 km and 2 km meshes has been used in [17].

3 Numerical evaluation

To estimate the effect of the different tracer placement on the formation of LKFs we solve a recently defined benchmark problem, which is briefly introduced further. A detailed description can be found in [17]. The test case considers the initial phase of sea ice deformation caused by a moving cyclone and compares the sea ice quantities after two simulated days. An idealized squared domain of the size $\Omega = (0, 512\,\text{km})^2$ is considered. The main force acting on the ice comes from a cyclonic wind stress pattern which moves from the midpoint to the north-east corner of the domain. The area ice is covered with a thin sea ice layer of approximately 30 cm. Using this benchmark problem we evaluate the shear deformation at different mesh resolutions. The analysis will be done first visually and then by applying the image detection algorithm described in [13]. More details on the setting of the algorithm can be found in [17].

We start with evaluating the edge-velocity staggering with tracers placed on vertices and cell centers. The discretization of these two cases is almost identical except for the placement of the tracers and the used advection scheme. In the case of cell placement we apply a first order upwind scheme, and the flux corrected transport scheme by [16] is used for tracers at vertices. A detailed information on the implementation is given in [17].

Figure 2 shows in the first and second column the resulting deformation fields produced with

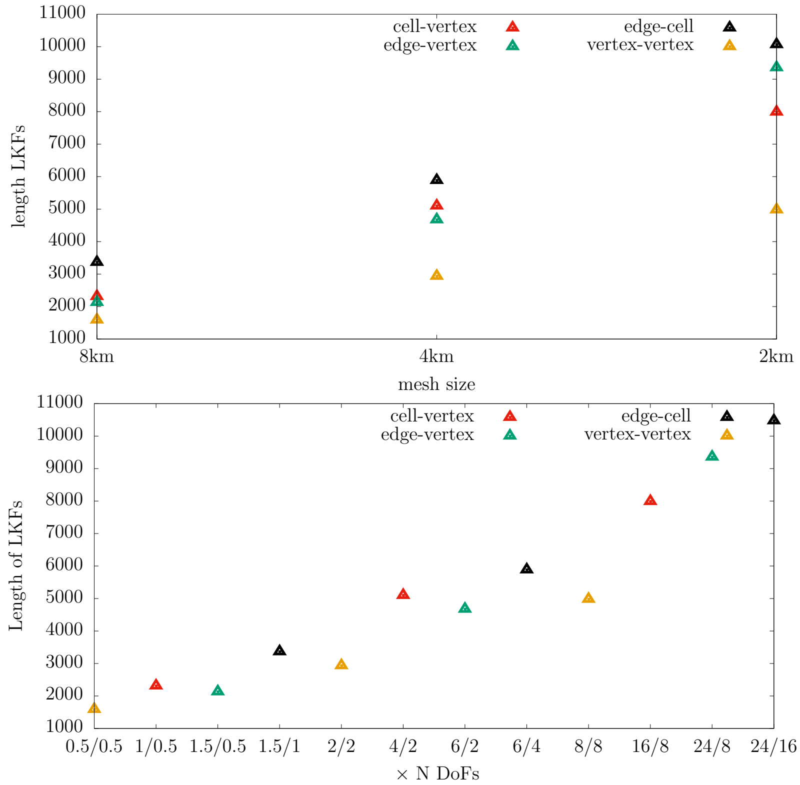

Figure 3: The detected total length with respect to the grid resolution (top) and the total length versus the degrees of freedom (bottom). In the bottom plot, the numbers refer to the DoFs in the velocity/tracer components, and N is the number of triangles of the 8 km mesh. The legend indicates the different velocity-tracer staggering.

.

these two different tracer placements combined the edge-based velocities. We observe that the simulation with a vertex-based tracer smooths out some LKFs. In the third column we keep the tracer placement and change the velocity staggering from the edge to the cell center. The change results in a sharper representation of the LKFs on the 4 km and 8 km mesh. Modifying the velocity placement from cell to vertex results in a strong smoothing of the LKFs.

These qualitative observations are supported by the output of the detection algorithm presented in Figure 3. The total length of LKFs with an edge-based velocity placement and a cell-placed tracer is much higher than for the edge-based velocity with a vertex-placed tracer. The algorithm indicates that the total length of the LKFs of the edge-vertex combination is even below the value of the cell-vertex setup on the 8 km and 4 km mesh. Focusing on the simulations with a vertex-based traces we observe that modifying the velocity staggering leads to a change of the amount of structure, which is consistent with the previous findings in [17]. In contrast to the previous study we also observe a strong increase of LKFs by changing the placement of the tracer and the advection scheme. The detection algorithm indicates that on coarse resolution meshes (8km and 4km) the relative effect of replacing the tracer degrees of freedom from vertex to cell is higher than placing the velocity from cell to edges. We will discuss this more in detail in Section 4.

4 Discussion and conclusion

In order to examine the effect of the tracer staggering on the formation of LKFs we compare the total length of all detected features and the visual evaluation of the shear deformation. We refrain from analyzing the total number of detected features as this quantity introduces some uncertainty. A feature which is intersected by another one can be wrongly counted as four instead of two features [17].

A previous analysis considering the same finite element discretizations on quadrilateral meshes concluded that the tracer staggering has a minor impact on the amount of produced LKFs compared to the effect of velocity placement [17]. A visual analysis of the shear deformation presented in Figure 2 however shows a clear influence of the tracer staggering on all mesh levels. As the benchmark problem is run only for a short time, the influence of the different advection scheme is minor and the observed effects can directly be attributed to staggering of the variables. The results demonstrate that in case of triangular grids the amount of LKFs is strongly related to the placement of the tracer on a triangle. The observation can be explained by the fact that the different tracer placements on triangular meshes have different total DoFs, while on quadrilateral grids the vertex and cell placement have the same number of DoFs. On triangular meshes the higher number of DoFs in the tracers results in a sharper representation of the sea ice strength in equation (10). The sea ice strength models the resistance of sea ice to compression and determines limit of compressive stress that sea ice withstands. By doing so the sea ice strength determines the length of the mayor axis of the elliptic yield curve in the viscous-plastic model. As a LKF is triggered once the stress state reaches the yield curve, the representation of the sea ice strength influences the formation of LKFs.

In the lower panel in Figure 3, we plot the detected length of LKFs with respect to the total number of DoFs available in the different setups. The graph shows that discretizations with a higher number of DoFs tend to increase the total length of LKFs. However, some setups resolve more structure on grids with less DoFs. For example the edge-cell placement resolves more LKFs than the vertex-vertex configuration even if the latter has more DoFs. The same is true for the cell-vertex setup on coarse meshes which produces more LKFs than the edge-vertex placement.

The fact that setups with less DoFs can resolve more LKFs can partly be explained by the size of the stencil. The stencil involves two triangles for the edge placement and 6 neighboring triangles for the vertex placement. For the cell placement, the computations of strain rates are done on vertices and edges, so that the stencil is undefined. The increased stencil introduces additional smoothing and suppresses the evolution of LKFs.

The edge-based velocity placement requires the use of a stabilization [18] which can be interpreted as discrete Laplacian. The stabilization scales with the length of a triangle and requires the choice of a parameter [18]. If the stabilization parameter is taken too large, too much smoothing is introduced, whereas a too low value causes oscillations. We guess that stabilization was not optimally selected in the case of the edge-vertex placement for lower resolutions, which is why less LKFs are resolved in these cases than with the cell-vertex setup. Since the stabilization scales with the length of the triangles, the refinement of the grid compensates for the too large choice of the stabilization parameter and the edge-vertex placement produces more LKFs on the 2 km mesh than the cell-vertex combination.

Figure 2 shows that with the respect to the total length of LKFs the relative effect of changing the velocity placement on coarse resolution (vertex to edge) is of similar magnitude as keeping the velocity staggering at edges and modifying the tracer staggering (vertex to cells). On the high resolution grid however varying the velocity placement clearly dominates the tracer variation, see upper panel of Figure 2. Tuning the stabilization parameter on different mesh levels might increase the amount of simulated LKFs with the edge-vertex discretization.

To conclude we observed that on triangular meshes the tracer staggering has a strong effect on the produced LKFs. The observation can be explained by the increased number of the degrees of freedom. The edge-based velocity placement produces more LKFs on meshes with fewer DoFs only in combination with a cell placed tracer. This highlights the importance of the tracer staggering on triangular meshes. Among the considered setups, the edge-based placement of the velocity in combination with the cell staggering of the tracers (CR-P0) is the preferable discretization on triangular meshes.

REFERENCES

[1] S. Bouillon, T. Fichefet, V. Legat, and G. Madec. The elastic-viscous-plastic method revisited. *Ocean Modelling*, 71:2–12, 2013.

[2] D. Braess. *Finite Elements: Theory, Fast Solvers, and Applications in Solid Mechanics.* Cambridge University Press, 3 edition, 2007.

[3] M.D. Coon, G.A. Maykut, R.S. Pritchard, D.A. Rothrock, and A.S. Thorndike. Modeling the pack ice as an elastic-plastic material. *AIDJEX Bull.*, 24:1–05, 1974.

[4] M. Crouzeix and P.-A. Raviart. Conforming and nonconforming finite element methods for solving the stationary Stokes equations. I. *Rev. Franc. Automat. Inform. Rech. Operat., R*, 7(3):33–76, 1974.

[5] S. Danilov, C. Mehlmann, and V. Fofonova. On discretizing sea-ice dynamics on triangular meshes using vertex, cell or edge velocities. *Ocean Modelling*, 170:101937, 2022.

[6] S. Danilov, Q. Wang, R. Timmermann, N. Iakovlev, D. Sidorenko, M. Kimmritz, T. Jung, and J. Schröter. Finite-Element Sea Ice Model (FESIM), version 2. *Geosci. Model Dev.*, 8:1747–1761, 2015.

[7] V. Dansereau, J. Weiss, P. Saramito, and P. Lattes. A maxwell elasto-brittle rheology for sea ice modelling. *The Cryosphere*, 10(3):1339–1359, 2016.

[8] L. Girard, S. Bouillon, J. Weiss, D. Amitrano, T. Fichefet, L. Thierry, and V. Legat. A new modeling framework for sea-ice mechanics based on elasto-brittle rheology. *Annals of Glaciology*, 52:123–132, 2011.

[9] H. Goosse, J.E. Kay, K.C. Armour, A. Bodas-Salcedo, H. Chepfer, D. Docquier, A. Jonko, P. J. Kushner, O. Lecomte, F. Massonnet, H.-S. Park, F. Pithan, G. Svensson, and M. Vancoppenolle. Quantifying climate feedbacks in polar regions. *Nat Commun*, 9(1919), 2018.

[10] W.D. Hibler. A dynamic thermodynamic sea ice model. *J. Phys. Oceanogr*, 9:815–846, 1979.

[11] E.C. Hunke and J.K. Dukowicz. An elastic-viscous-plastic model for sea ice dynamics. *J. Phys. Oceanogr.*, 27:1849–1867, 1997.

[12] N. Hutter and M. Losch. Feature-based comparison of sea ice deformation in lead-permitting sea ice simulations. *The Cryosphere*, 14(1):93–113, 2020.

[13] N. Hutter, L. Zampieri, and M. Losch. Leads and ridges in arctic sea ice from rgps data and a new tracking algorithm. *The Cryosphere*, 13(2):627–645, 2019.

[14] Nils Hutter. lkf_tools: a code to detect and track Linear Kinematic Features (LKFs) in sea-ice deformation data (Version v1.0), 2019. Zenodo.

[15] J H Jungclaus, S J Lorenz, H Schmidt, V Brovkin, N Brüggemann, F Chegini, P De-Vrese, V Gayler, M A Giorgetta, O. Gutjahr, H Haak, S Hagemann, M Hanke, T Ilyina, P Korn, J Kröger, L Linardakis, C Mehlmann, U Mikolajewicz, W A Müller, J E M S Nabel, D Notz, H Pohlmann, D Putrasahan, T Raddatz, L Ramme, R Redler, C H Reick, T Riddick, T Sam, R Schneck, R Schnur, M Schupfner, J-S von Storch, F Wachsmann, K-H Wieners, F Ziemen, B Stevens, J Marotzke, and M Claussen. The icon earth system model version 1.0. *J. Adv. Model. Earth. Sy.*, 2022.

[16] R. Löhner, K. Morgan, J. Peraire, and M. Vahdati. Finite-element flux-corrected transport (FEM-FCT) for the Euler and Navier–Stokes equations. *Internat. J. Numer. Methods Fluids*, 7:1093–1109, 1987.

[17] C. Mehlmann, S. Danilov, M. Losch, J. F. Lemieux, N. Hutter, T. Richter, P. Blain, E. C. Hunke, and P. Korn. Simulating Linear Kinematic Features in Viscous-Plastic Sea Ice models on quadrilateral and triangular Grids With Different Variable Staggering. *Journal of Advances in Modeling Earth Systems*, 13(11):e2021MS002523, 2021.

[18] C. Mehlmann and P. Korn. Sea-ice dynamics on triangular grids. *J. Comput. Phys.*, 428:110086, 2021.

[19] M. Mohammadi-Aragh, F. H. Goessling, M. Losch, N. Hutter, and T. Jung. Predictability of Arctic sea ice on weather time scales. *Scientific Reports*, 8, 2018.

[20] M. Petersen, X. Asay-Davis, A. Berres, Q. Chen, N. Feige, M. Hoffman, D. Jacobsen, P. Jones, M. Maltrud, S. Price, T. Ringler, G. Streletz, A. Turner, L. Van Roekel, M. Veneziani, J. Wolfe, P. Wolfram, and J. Woodring. An Evaluation of the Ocean and Sea Ice Climate of E3SM Using MPAS and Interannual CORE-II Forcing. *Journal of Advances in Modeling Earth Systems*, 11(5):1438–1458, 2019.

[21] P. Rampal, S. Bouillon, E. Olason, and M. Morlighem. neXtSIM: a new lagrangian sea ice model. *The Cryosphere*, 10:1055–1073, 2016.

[22] R. Timmermann, S. Danilov, J. Schröter, C. Boening, D. Sidorenko, and K. Rollenhagen. The Finite Element Sea Ice-Ocean Model (FESOM) v.1.4: formulation of an ocean general circulation model. *Geosci. Model Dev.*, 7:663–693, 2014.

[23] M. Tsamados, D. L. Feltham, and A. V. Wilchinsky. Impact of a new anisotropic rheology on simulations of arctic sea ice. *Journal of Geophysical Research: Oceans*, 118(1):91–107, 2013.